

Mode mixity and fracture in pull-off adhesion tests

Heather P.H. Liddell^{a,*¹}, Laura M. Erickson^b, James P. Tagert^c, Attilio Arcari^c, Gregory M. Smith^{c,2}, James Martin^c

^a American Society for Engineering Education – U.S. Naval Research Laboratory, Code 6354, Washington, DC, USA

^b Rampart, LLC, Falls Church, VA, USA

^c Center for Corrosion Science and Engineering, U.S. Naval Research Laboratory, Code 6130, Washington DC, USA



ARTICLE INFO

Keywords:
 Mode mixity
 Fracture mechanics
 Delamination
 Fracture patterns
 Crack kink angle
 ASTM D4541
 Adhesion testing
 Pull-off adhesion
 Trainable WEKA

ABSTRACT

Following pull-off coating adhesion tests such as ASTM D4541, visual examination of the fracture surfaces often reveals intriguing fracture patterns where similar (and seemingly predictable) features are observed across like coating systems. Nonetheless, adhesion test stubs are typically discarded after a brief visual inspection or no inspection at all—suggesting a missed opportunity to gain further insight into fracture processes. This paper examines the pull-off adhesion test from a fracture mechanics perspective. We present two microscopy-based methods for extracting analytically useful fracture data from pull-off adhesion tests. First, we develop an energy-based method for obtaining mode mixity from observed crack kink angles, providing the powerful capability to disambiguate mode I and mode II fracture. We demonstrate agreement between experimental results and theoretical predictions in a set of 1,305 crack path measurements for 111 pull-off adhesion test stubs, representing both single- and multi-layered coating systems. Second, we deploy a machine-learning based image segmentation technique (Trainable WEKA) to rapidly quantify the fractional area coverage of materials removed with the pull stub, enabling further insight into the surfaces most vulnerable to delamination in a layered coating stack. Beyond the immediate utility of these techniques for data enhancement in pull-off adhesion tests, these techniques also have long-term potential as tools for failure analysis in coated systems.

1. Introduction

In a standard ASTM D4541 pull-off adhesion test [1], illustrated in Fig. 1, a pull stub or “dolly” is attached to a coated substrate and then removed through vertical loading. The force required to separate the coating from its substrate provides a measure of its adhesion strength. While pull-off adhesion tests provide a convenient, standardized, and rapid technique for evaluating the adhesion strength of a paint or coating to an underlying substrate, these tests have not generally provided the basis for a deeper fracture mechanics understanding. Yet visual examinations of used pull stubs reveal predictable, characteristic fracture patterns for like substrate conditions and coating systems. This suggests a missed opportunity to draw further insight into fracture processes through systematic visual inspection and measurement of fracture surfaces.

In this article, we approach the pull-off adhesion test from a fracture mechanics perspective. We develop a simple theoretical model

* Corresponding author.

E-mail address: heather@liddellanalytics.com (H.P.H. Liddell).

¹ Present address: Liddell Analytics, LLC, Washington DC, USA; and Energetics, Washington DC, USA.

² Present address: Azimuth Technical Consultants, Inc., Sugarloaf Key, FL, USA.

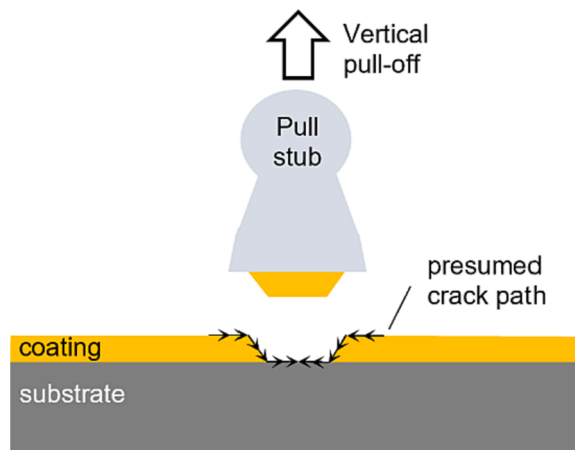


Fig. 1. Schematic depiction of an ASTM D4541 stub pull-off adhesion test.

for mixed-mode fracture which is validated through experimental measurements of crack paths. Based on experimental results, we propose two new microscopy-based methods for extracting analytically useful data from pull-off adhesion test stubs:

- First, we present a technique for back-calculating the mode mixity of fracture from experimental measurements of the crack path (specifically, the crack kink angle θ). This technique provides the powerful capability to disambiguate mode I / mode II fracture post hoc, without prior knowledge of loading conditions.
- Second, we demonstrate the use of machine-learning-based image segmentation (Trainable WEKA [2]) to inspect and quantify the fractional area coverage of coating layer(s) on used pull stubs, providing further insight into the roles of each material in the fracture process.

Both techniques are demonstrated for single- and multi-layer coating systems. These simple-to-use techniques demonstrate a substantial enhancement in the richness of data available from pull-off adhesion tests. Further, similar techniques and principles can be applied to the analysis of delamination fracture surfaces more generally—whether those fracture surfaces are experimentally induced or result from a spontaneous failure. Beyond applicability to pull-off adhesion testing, similar methods can be incorporated into the failure analyst's toolbox across a wide range of applications involving coating fracture, delamination, and other adhesion problems. Useful applications could include forensic estimation of loading conditions leading to coating failure; disambiguation of failure modes and local mode mixities in multi-layered systems; prediction of preferred crack propagation paths for known material/loading combinations; and design of failure-tolerant coatings that mitigate catastrophic adhesion failure through mechanical property tailoring and/or crack steering.

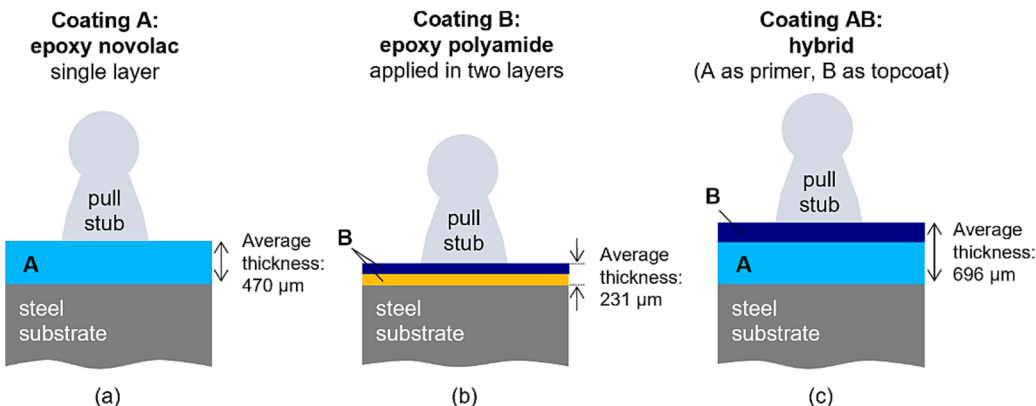


Fig. 2. Schematic depiction (not drawn to scale) of the three coating systems tested: (a) "Coating A" – a single-layer epoxy novolac amine system; (b) "Coating B" – an epoxy polyamide system applied in two nearly identical layers; and (c) "Coating AB," a two-layer hybrid system consisting of a base layer of Coating A followed by a topcoat of Coating B.

2. Materials and methods

2.1. Coating systems and properties

Three epoxy-based marine coating systems were selected as the focus of this study:

- Coating A: a single-layer epoxy novolac amine system (98 % solids) with an average thickness of 470 μm ;
- Coating B: a two-layer epoxy polyamide system (67 % solids), applied as a primer and topcoat, with an average total thickness of 231 μm ; and
- Coating AB: a two-layer system consisting of a single-layer base layer of Coating A (231 μm) and a topcoat of Coating B (465 μm), with a combined average thickness of 696 μm .

These three coatings are schematically illustrated in Fig. 2 and their estimated material properties are shown in Table 1. Elastic modulus E for the coating materials was measured through free-film tensile testing (Testometric load frame, 250 kgf load cell) in accordance with the ASTM D882 test method [3]. Coatings were sprayed onto silicone release paper to allow for removal and tensile testing as a free film, and at least 5 replicates were tested per material at a cure time of 60 days to measure the elastic modulus. Coatings A and B were both brittle epoxy resins, well below their glass transition temperature at room temperature, and exhibited a strain of less than 3 % at break during tensile testing. For Coating A, Poisson's ratio ν was measured using the digital image correlation (DIC) method, again using free-film samples. Free-film specimens of Coating B were unavailable for Poisson's ratio testing, and therefore Poisson's ratio for Coating B was estimated based on engineering judgment for this epoxy-polyamide material including a literature review (see e.g., Refs. [4–6], each of which reports a Poisson's ratio between 0.34 and 0.35 for polyimide resin; data for epoxy polyamides could not be found). Standard literature values for aluminum were also assumed. Shear modulus $\mu = E/[2(1 + \nu)]$ was calculated from E and ν through the standard formula for isotropic materials, and the uncertainty for experimental values of E and ν was propagated to generate an error estimate for μ . Since an experimental value for Poisson's ratio of Coating B was not available, an uncertainty of 10 % for the literature value was applied in error propagation calculations. Coating B was treated as a single-layer coating analytically because the primer (first layer) and topcoat (second layer) were composed of the same polymer, though tinted in different colors. Differences in mechanical properties for the Coating B primer and topcoat were assumed to be negligible.

All coatings were deposited onto steel substrates having dimensions of 152 mm \times 305 mm \times 6 mm (6" \times 12" \times 1/4"). Steel substrates were prepared by abrasive blasting with aluminum oxide size 24 abrasive to produce a surface roughness profile of 50 to 100 μm . Coatings A (single layer) and B (both layers) were deposited using an industrial airless spray gun. The topcoat of Coating B was deposited during the manufacturer-specified overcoat window, prior to a full cure for the base coat, to increase interfacial bonding. In Coating AB, the base layer of Coating A was deposited using airless spray equipment, and the topcoat of Coating B was deposited atop Coating A using a drawdown bar method with an automatic film applicator following a full cure of Coating A. All coatings were cured according to manufacturer recommendations.

After curing, coated panels were lightly scuff-sanded and 20-mm-diameter aluminum pull stubs (DeFelsko Inspection Instruments model DOLLY20) were affixed to the coated surfaces using a two-part epoxy adhesive (3 M Scotch-Weld DP460, off-white) following manufacturer instructions. Excess adhesive was wiped away with a cotton swab. Coatings were not "scored" around the edges of the stub to separate the test area from the surrounding coating. (While scoring is permitted in ASTM D4541, it is considered a deviation from the standard test method and would plainly obstruct the crack path experiments being carried out here.) The minimum center-to-center spacing between adjacent stubs was 51 mm (2 in.). In total, 144 pull stubs (12 stubs per panel \times 4 panels per coating system \times 3 coating systems) were adhered to the coated test panels and prepared for testing.

Following preparation, coated panels (with pull stubs adhered) were subjected to a range of environmental and mechanical conditions in the laboratory for a period of up to eight months to "pre-stress" coatings prior to adhesion testing, simulating variations in real-world conditions. Treatment conditions included water exposure, coating aging, and mechanical loading, with all being imposed at room temperature. For the purposes of this paper, results have been aggregated across these pre-stress treatment conditions and we will not analyze their effects here except to note that:

- (1) imposed pre-stress treatments were identical for all coating systems (i.e., the same number of specimens from each coating system was subjected to each treatment); and

Table 1
Material properties of coatings and pull stubs: elastic modulus E , Poisson's ratio ν , and shear modulus μ .

	E (GPa) (avg. \pm S.D.)	ν (avg. \pm S.D.)	μ (GPa) (Calculated)	Data sources
Coating A (epoxy novolac amine)	1.20 \pm 0.10	0.31 \pm 0.02	0.46 \pm 0.05	Experimental E and ν (this work).*
Coating B (epoxy polyamide)	1.01 \pm 0.20	0.34 (\pm 0.03)	0.38 \pm 0.07	Experimental E (this work) and estimated ν (literature).*
Pull stub (aluminum)	69.0	0.30	26.5	Standard values for E and ν (literature).

* Error from E and ν was propagated to μ . For Coating B, since experimental data for ν were unavailable, a 10% uncertainty in ν was applied in propagation-of-error calculations for μ .

(2) effects of the pre-stress treatments on tensile strength, crack kink angle, and other measurements were generally found to be small.

2.2. Adhesion testing

Initially, we planned to perform adhesion tests using an ASTM D4541-compliant portable hydraulic adhesion tester (PosiTec AT-M, DeFelsko Inspection Instruments) following the ASTM D4541 methodology [1]. However, it was quickly determined that the coatings included in this study were strongly adhered and beyond the measurement capability of the instrument. We removed only a single pull stub using the DeFelsko portable adhesion tester; all others that were attempted exceeded the maximum pressure load of the device. Subsequently, we sought alternative methods for removing the pull stubs in a manner consistent with ASTM D4541 and Fig. 1. Two alternative methods were developed.

In one method, a universal test machine (Baldwin/Satec BTE) was used to remove the pull stubs in tension, clamping the panels to the machine stage with three large “C” clamps and securing the stub in a quick-connect fixture connected to the upper machine grip. We successfully removed a total of eleven pull stubs using this method, but variance was high and we had concerns about panel flexure during testing, which was substantial enough to be noted visually. Unlike in the portable adhesion tester, where the panel is secured circumferentially around the pull stub with the hydraulic actuator stand-off device itself, in the Baldwin setup the panel had to be secured by clamping, with the pull stub manually aligned. The clamping location varied to accommodate the location of the pull stub on the panel. We believe that differences in clamping constraints led to different levels of panel bending, ultimately affecting the results. We decided to exclude tests performed using this method from our results.

The second alternative adhesion test method, designated here as the “torque-wrench method,” was designed to emulate ASTM D4541 through a custom, portable mechanical device [7]. The pull stub was secured in a quick-connect coupler with a central threaded post, which was enclosed in a housing consisting of a polyvinyl chloride (PVC) standoff ring sitting flush to the panel. Finally, a sequence of washers and a nut were threaded onto the post, securing the PVC ring such that loads could be transmitted through it during stub removal. A digital torque wrench was used to apply loading through the nut, pulling the stub away from the panel in a vertical loading. This method, illustrated schematically in Fig. 3, enabled higher overall removal loads than the DeFelsko hydraulic instrument. (Another unique feature of this method is that the loading fixture can remain in-place on the panel over extended periods, with or without environmental exposures, to provide long-term “creep” loadings below the failure load. This special feature will not be explored in this paper, but will be a focus of future work.).

The torque-wrench adhesion test method proved effective and repeatable in this experimental study, and was deployed for all remaining tests (127 experiments in all, after excluding the 11 pull stubs for which the Baldwin machine was used, 1 pull stub that was successfully removed with the DeFelsko portable adhesion tester, and 5 other pull stubs that could not be measured due to testing failures). Results for the 127 pull stubs successfully removed using the torque-wrench method (out of the original 144 pull stubs) comprise the dataset analyzed in this article, with the stubs removed by other methods excluded to avoid confounding results.

To relate the removal load in the custom torque-wrench method to an equivalent ASTM D4541 removal load, we performed a series of 30 paired replicate adhesion tests (i.e., 15 tests using the DeFelsko instrument following the ASTM D4541 method and 15 identical tests using the custom torque-wrench method) on samples of ten different epoxy-based coatings on steel substrates. These test coatings, unrelated to the primary sample set of this study, exhibited adhesion strengths in the range measurable using both techniques. The relationship between the removal loads measured using the two methods for each replicate pair was linear, as shown in Fig. 4. The linear relationship between removal load and torque is physically consistent with bolt theory, and the coefficient agreed approximately (within 25 %) with a rule-of-thumb based estimation based on the bolt torque-force relationship (see, e.g., *Shigley's Mechanical Engineering Design* [8]). The linear regression fit shown in Fig. 4 was extrapolated to estimate the ASTM D4541-equivalent removal load for all tests performed in this study.

Adhesion tests were performed over a period of eight months, with test dates determined by the duration of the pre-stress treatments described in the previous section. Test order was randomized across panel and stub position for each coating system in advance of testing. The measured pull-off load (converted to ASTM D4541-equivalent, as noted above) was about 32 MPa for all three coating systems, with nearly identical average and standard deviation results for each system (32.4 ± 7.7 MPa, 31.7 ± 6.9 MPa, and 32.8 ± 7.3 MPa for Coating A, B, and AB respectively). Differences in adhesion strength measurements across coatings were not statistically significant, as evident from the data and confirmed by a one-way ANOVA.

2.3. Microscopy of pull stubs

Following adhesion testing, each used pull stub was imaged in two orientations (Fig. 5). Top-down micrographs, which allowed visualization of the fracture pattern and failure interfaces, were captured using a Nikon SMZ 1500 stereo microscope. Four quadrant micrographs were stitched together to generate a complete composite image of each 20-mm-diameter pull stub. Side-on micrographs, which allowed visualization of the crack path and measurement of the crack angle (near the perimeter of the pull stub), were captured using a horizontally mounted Navitar 12x zoom lens. The pull stub was dual-illuminated, including back-lighting from behind the pull-

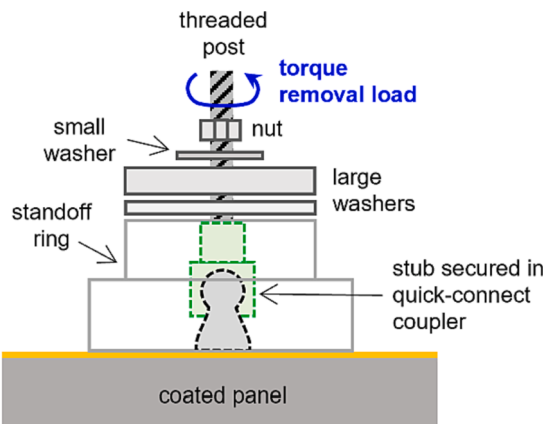


Fig. 3. Schematic of custom torque-wrench adhesion test method, designed to emulate the loading conditions of ASTM D4541 while allowing for higher removal loads.

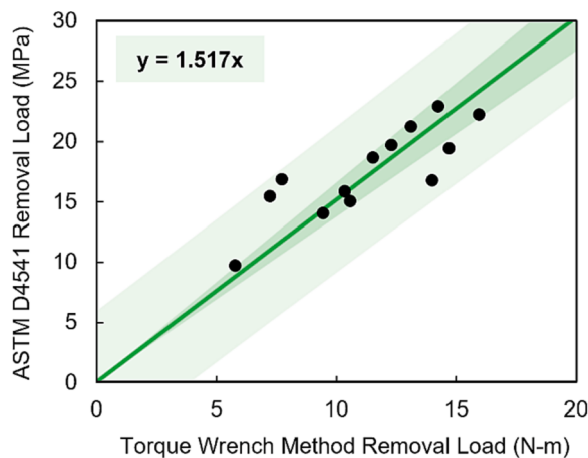


Fig. 4. Relationship between removal loads as measured with ASTM D4541 and the torque-wrench method, shown with a zero-intercept linear regression fit. Shaded intervals show the 95% confidence interval for the regression (narrow band) and the 95% prediction interval for individual values (broader band).

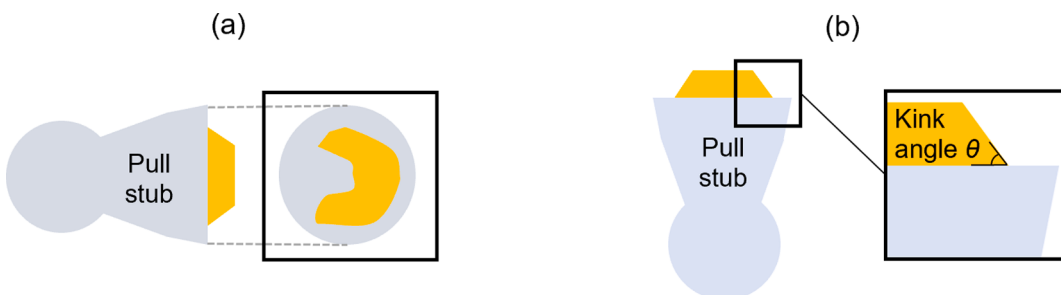


Fig. 5. Imaging configurations for inspection of pull stubs in two orientations: (a) top-down, exposing the fracture surfaces; and (b) side-on, exposing the angular crack path as it kinks from the interface into the coating.

stub and front-lighting from the camera side, with a pair of light emitting diodes to clearly illuminate the crack kink angles as well as the layer breakpoints from the aluminum pull stub to adhesive (glue) and coating layers. For each micrograph, the crack kink angle was digitally measured in ImageJ by manually selecting vertices.³ The authors note that the Navitar zoom lens setup in our laboratory was originally designed for contact angle measurements [9], but this simple system has proven versatile for “perpendicular view” microscopy across many other types of experiments, including silhouette microscopy and roughness measurement, and is further described elsewhere [10,11]. In other laboratories, we expect that other self-built or commercial contact angle measurement setups could be adapted with minimal modification for similar results.

2.4. Image segmentation via Trainable WEKA

Since ASTM D4541 requires pull-to-failure, fracture necessarily propagates across the entire stub in any given test—but failure might occur at any combination of materials and interfaces. Clearly, fracture at certain interfaces is more problematic than others. If fracture most frequently occurs at the substrate/coating interface, resulting in a large portion of the coating being removed with the pull stub, this might suggest a coating that is relatively susceptible to delamination. Conversely, if fracture most often occurs cohesively within the coating layer, or at the “glue” interface of the epoxy adhesive with the pull stub, this suggests a strongly adhered coating. Image segmentation provides a convenient and rapid technique for quantitatively assessing and comparing failure interfaces observed in a coating system.

To quantify the fractional area occupied by each material on the pull stubs, Trainable WEKA (a machine-learning-based image segmentation plug-in for ImageJ [2]) was deployed. A custom “classifier” was trained for each coating system, and the trained classifiers were then applied in a batch process to segment all images. Fig. 6 shows one example of a classification protocol applied to a training image for Coating AB. Classifiers were trained by manually selecting areas representing each material on each training image, and iterating (by adding additional training images) until accurate segmentation of an arbitrary image was demonstrated.

3. Fracture mechanics Theory: Mixed-Mode loading in Pull-Off adhesion tests

3.1. Theory and calculations

In an ASTM D4541 pull-off adhesion test, the applied force is expected to be mostly vertical, as depicted in Fig. 1. Nonetheless, the end result is a mixed-mode loading as a result of the mismatch in material properties across the interfaces. For the fracture mechanics model, we assume a crack that begins at the outer perimeter of the pull stub. As the vertical removal force is applied, the crack may propagate initially along the coating/stub interface if energetically favorable (i.e., pulling off the stub without separating the coating from its substrate), but in most cases the crack eventually kinks downward through the coating at angle θ , and some amount of coating is removed with the stub.

He and Hutchinson [12] showed that for an interfacial crack between dissimilar media, the ratio of the energy release rate for a kinked crack, G , and that of a crack advancing in the interface, G_0 , is given by equation (1):

$$\frac{G}{G_0} = \frac{|c|^2 + |d|^2 + 2 \operatorname{Re}[cd\exp(2i\bar{\psi})]}{\sqrt{(1 - \beta^2)/(1 + \alpha^2)}}, \quad (1)$$

where α and β are the Dundurs material-mismatch parameters, which depend on the shear moduli (μ_1, μ_2) and Poisson’s ratios (ν_1, ν_2) of the interfacing materials. The Dundurs parameters are given by equations (2) and (3) for plane-strain conditions (which are applicable to interfaces with a large mismatch between elastic constants; see, e.g., Ref. [13]):

$$\alpha = \frac{\mu_1(1 - \nu_2) - \mu_2(1 - \nu_1)}{\mu_1(1 - \nu_2) + \mu_2(1 - \nu_1)}; \quad (2)$$

$$\beta = \frac{1}{2} \left[\frac{\mu_1(1 - 2\nu_2) - \mu_2(1 - 2\nu_1)}{\mu_1(1 - \nu_2) + \mu_2(1 - \nu_1)} \right]. \quad (3)$$

The mode-mixity angle ψ describes the crack loading, and is defined as $\psi = \tan^{-1}(K_{II}/K_I)$, where K_I and K_{II} are the mode-I (opening) and mode-II (shearing) stress intensity factors, respectively. The corrected mode-mixity $\bar{\psi}$ appearing in equation (1) is adjusted for the problem length scale as

$$\bar{\psi} = \psi + \varepsilon \ln(a/h), \quad (4)$$

where a is the crack length, h is the coating thickness, and ε is the bimaterial constant given by

³ We also explored the use of contact profilometry to measure the crack kink angles, but this was found to be substantially more time-intensive than the imaging method, so it was discontinued. However, such a technique may still be useful for “interior” crack kink angles (i.e., for measuring cracks with locations other than at the outer perimeter of the pull stub, where the angle would not be visible using a perpendicular imaging system).

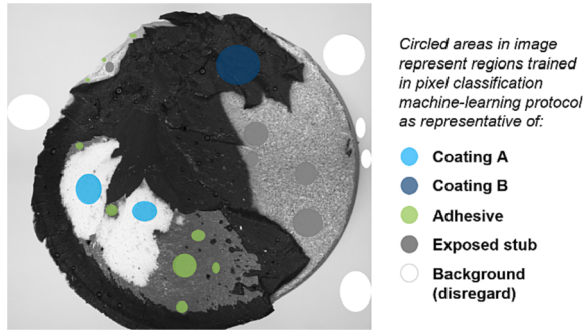


Fig. 6. Example of pixel classification training (for Coating AB) in Trainable WEKA for ImageJ.

$$\varepsilon = \frac{1}{2\pi} \ln\left(\frac{1-\beta}{1+\beta}\right). \quad (5)$$

The quantities c and d in equation (1) are complex-valued functions that depend on α , β , and θ , and have been tabulated by He and Hutchinson as a function of θ [14].

Based on equation (1), we can express G/G_0 as a function of crack kink angle θ and mode-mixity angle ψ . Equation (1) does not predict whether the crack will indeed propagate, as it does not include a fracture criterion, but it can predict the preferred angular path should the crack advance. When $G/G_0 > 1$, the crack may prefer to kink into the coating rather than continuing along the interface, particularly if the coating is significantly more compliant than the substrate and/or less tough than the interface [12,15]. If a local maximum of G/G_0 exists for a non-zero value of θ , we interpret this as an energetically favorable kink angle. Thus, if loading conditions (and thus the mode-mixity angle ψ) are known, we can calculate the preferred kink angle by identifying the maximum of the G/G_0 curve. Conversely, if experimental measurements of crack kink angles are known, we can back out an estimate of the mode-mixity angle ψ by assuming fracture consistent with the most energetically favorable crack path. A similar approach was taken in earlier work by one of the authors [16] for a different material system (a multilayer metal oxide coating on glass).

Modeling the stub/coating system as a bilayer held between rigid grips, shown in Fig. 7, we estimated the mode-mixity angle $\psi(\alpha, \beta)$ by interpolating over Hutchinson and Suo's numerical data for this setup [17]. We correct for length scale by assuming a crack length a equal to the thickness of the coating layer in which the crack advanced, and a coating thickness h equal to the thickness of the overall coating stack ahead of the crack.

The calculated mode-mixity angles $\psi(\alpha, \beta)$, length scale a/h , and corrected mode-mixity angles $\bar{\psi}(\alpha, \beta)$ resulting from these analytical assumptions are shown in Table 2 for the material interfaces considered in this work. There is only one relevant interface for the single-layer coatings A and B, but two relevant interfaces for the multilayer system AB because the crack kinks into the coating first at the stub/coating interface (stub to B) and then again at the interlayer interface (B to A). The length scale a/h differs in these two cases. As the crack begins to advance through the first layer (stub to B), we take the ratio of the thickness of the Coating B layer to the total Coating AB stack ($a/h = 0.33$) as the length scale. However, when the crack kinks from Coating A to Coating B, only a single layer remains for the crack to traverse, and therefore the length scale a/h is unity.

For the B to A interface in Coating AB, rule of mixtures was used to assess material properties of Material #1 in the bilayer system, considering contributions from both Coating B as well as the underlying aluminum pull stub. This was justified by the idea that an advancing crack, traveling from Coating B to Coating A, would "feel" not only the properties of the coatings, but also those of the thick and stiff aluminum pull stub, considering that Coating B was quite thin compared to the length scale of cracking in Coating A. For the

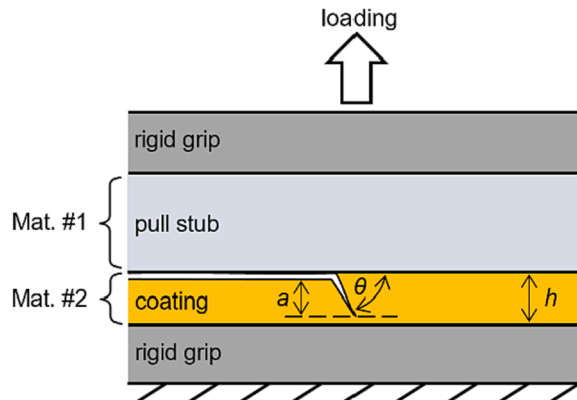


Fig. 7. Pull stub/coating system modeled as a bilayer held between rigid grips, after Hutchinson and Suo [17].

Table 2

Analytical results for mode-mixity, length-scale corrections, and energetically preferred crack kink angles for each material interface.

System	Interface	Material #1	Material #2	Calculated mode mixity $\psi(\alpha, \beta)$	Length scale a/h	Corrected mode mixity $\bar{\psi}(\alpha, \beta)$	Predicted crack kink angle θ_p
A	Stub to A	Al stub	Coating A	15.3°	1.00	15.3°	34.1°
B	Stub to B	Al stub	Coating B	18.0°	1.00	18.0°	38.2°
AB	Stub to B	Al stub	Coating B	18.0°	0.33	22.8°	43.7°
AB	B to A	Coating B / Al stub*	Coating A	14.1°	1.00	14.1°	32.4°

* Rule of mixtures was used to assess effective properties for Material #1 with contributions from both Coating B and the underlying aluminum stub, with the overall depth of the combined layer (for purposes of estimating effective material properties) assumed to be equal to the length scale of the advancing crack a .

rule-of-mixtures calculations, it was necessary to assess a depth of interest in the Coating B / aluminum combined layer to determine the volume fraction of each material that should be included in the mixture to calculate effective properties. Noting uncertainty in this estimate, we assumed a depth equal to the length scale of the crack (in this case, the thickness of the Coating A layer). Since the average layer thicknesses were 465 μm and 231 μm for Coating A and B respectively, the rule-of-mixtures calculations for the Coating B / aluminum combination accounted for 231 μm of Coating B and 234 μm of aluminum for a total thickness of 465 μm . Since rule-of-mixtures calculations provide upper and lower bounding values for modulus rather than a single estimate, the lower and upper limits were averaged to estimate a single combined modulus of the Coating B / aluminum stub mixture ($E = 18.6 \text{ GPa}$).

For each interface, the preferred crack kink angle θ_p was determined by identifying the angle that maximizes the energy release rate ratio G/G_0 for the kinked crack based on the mode mixity $\bar{\psi}(\alpha, \beta)$ based on equation (1). Theoretical energy release rate curves, plotted in Fig. 8, show that the analytically predicted preferred crack kink angles range from 32.4° and 43.7° for the four material interfaces studied here.

3.2. Sensitivity analysis

The theoretical estimations of energetically optimal crack kink angle θ_p (Table 2 and Fig. 8) depend on the material properties E and ν of the interfacing materials, which control the Dundurs parameters α and β as well as the bimaterial constant ϵ . For the coating materials A and B, the values of E and ν are subject to experimental errors. A sensitivity analysis was conducted to understand the effect of potential variations in material properties E_A , E_B , ν_A , and ν_B on the analytical prediction of the preferred crack angle θ_p . For each interface, we assessed the effects of independently varying the value of either E or ν by $\pm 10\%$ or $\pm 25\%$. The actual experimental error in E and ν was estimated at 8–19 % and 7–10 % respectively (Table 1), so it is expected that the $\pm 10\%$ sensitivity band for Poisson's ratio ν should capture potential variation in ν , whereas the $\pm 25\%$ sensitivity band for Young's modulus E should capture potential variation in E . Results of the sensitivity analysis are shown in Table 3. Analytical predictions of the preferential crack path were found to be most sensitive to the assumed Poisson's ratio for the coating layer in which the crack is propagating (9–13 % difference in predicted θ_p when varying ν by $\pm 10\%$), and only weakly sensitive to Young's modulus (less than 2 % difference in predicted θ_p when varying E by $\pm 25\%$). These results are illustrated graphically in Fig. 9.

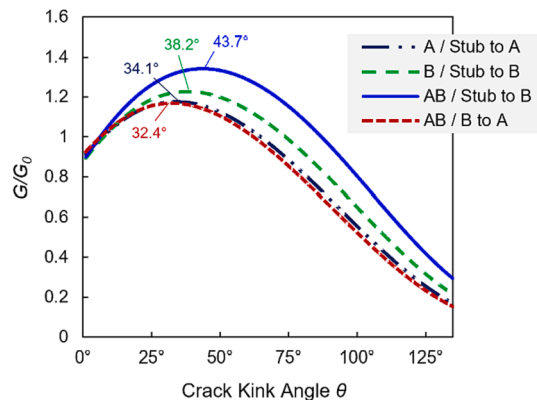


Fig. 8. Energy release rate ratio G/G_0 plotted as a function of crack kink angle θ , annotated with the energetically preferred crack kink angle θ_p (located at the peak value of G/G_0) for each material interface.

Table 3Sensitivity of Analytical Crack Path Predictions to Variation in Young's Modulus E and Poisson's Ratio ν .

		Preferred crack kink angle θ_p									
		Varying E_A					Varying ν_A				
System	Interface	-25 %	-10 %	0 %	+10 %	+25 %	-25 %	-10 %	0 %	+10 %	+25 %
A	Stub to A	34.2°	34.1°	34.1°	34.1°	33.9°	26.2°	30.6°	34.1°	38.0°	45.1°
AB	A to B	32.9°	32.6°	32.4°	32.0°	31.9°	26.2°	29.7°	32.4°	35.3°	40.9°
		Varying E_B					Varying ν_B				
System	Interface	-25 %	-10 %	0 %	+10 %	+25 %	-25 %	-10 %	0 %	+10 %	+25 %
B	Stub to B	38.2°	38.2°	38.2°	37.9°	37.9°	28.2°	33.7°	38.2°	42.9°	51.5°
AB	Stub to B	43.7°	43.7°	43.7°	43.4°	43.4°	33.4°	39.1°	43.7°	48.3°	56.1°
AB	A to B	32.2°	32.4°	32.4°	32.4°	32.4°	32.5°	32.3°	32.4°	32.3°	32.2°

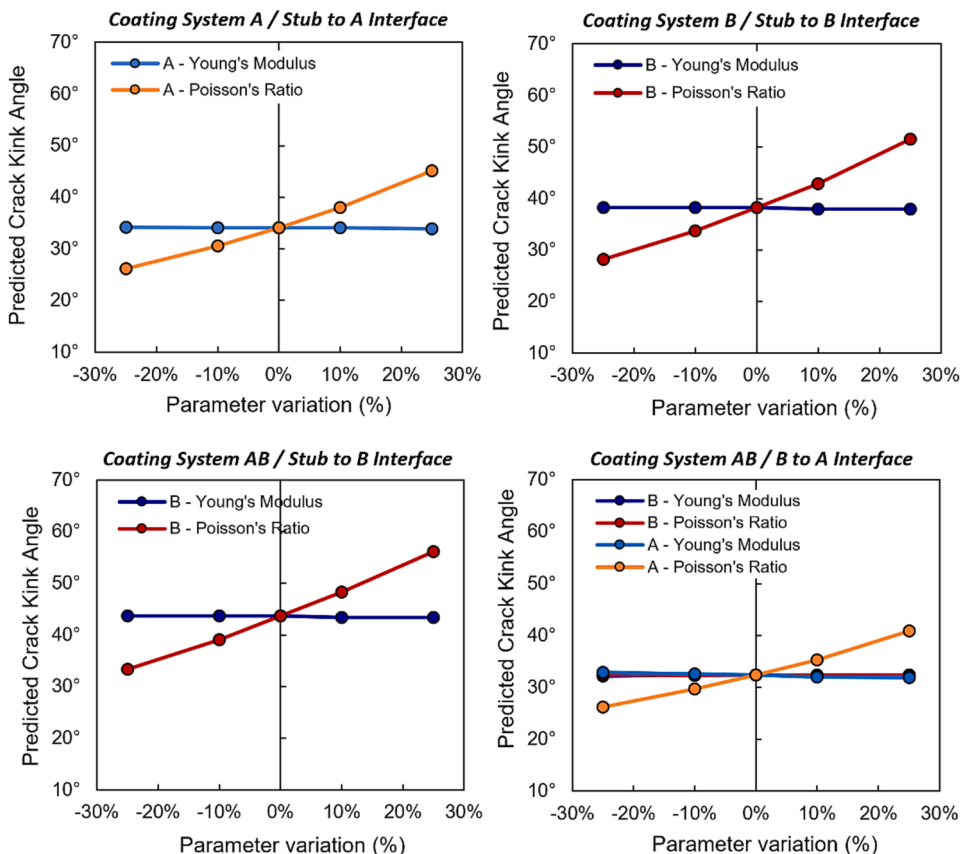


Fig. 9. Sensitivity of analytical predictions of crack kink angle to the assumed values of Young's modulus E and Poisson's ratio ν for the coating materials. Analytical predictions were most sensitive to the Poisson's ratio of the coating layer in which the crack is advancing, and only weakly sensitive to Young's modulus.

Table 4

Analytically predicted and experimentally measured crack kink angles.

System	Interface	Analytical θ_p (with sensitivity bands)	Experimental θ_p (pooled mean \pm S. D.)	n_{pooled} (number of stubs measured)	n_{measured} (total number of measurements)	% Difference Between Experimental and Analytical
A	Stub to A	34.1° \pm 3.9°	31.3° \pm 3.8°	39	311	- 8.1 %
B	Stub to B	38.2° \pm 4.7°	35.6° \pm 9.4°	30	394	- 6.7 %
AB	Stub to B	43.7° \pm 4.6°	44.9° \pm 7.9°	41	277	+ 2.8 %
AB	A to B	32.4° \pm 2.7°	27.9° \pm 5.3°	42	323	- 13.8 %

4. Experimental results: crack kink angles, mode mixity, and fracture patterns

4.1. Experimental prediction of mode mixity from crack paths

A representative sample of side-view pull stub images for each coating system are presented in Fig. 10. Pull stubs were inverted (placed on the stage coating-side-up) for accurate imaging, and angular measurements were made manually in ImageJ software by selecting three points in each image to define the vertices. Several measurements were made for each pull stub at different locations by rotating the pull stub on the stage. As shown in the images, the crack typically kinked into the coatings close to the edge of the pull stub (after advancing in the interface for a short distance, or not at all) – but the distance between the edge of the stub and the point where the crack kinked into the coating varied from system to system and stub to stub. In the two-layer Coating AB system, we observed that the crack kinked almost immediately into the top layer of Coating B (near the stub perimeter), but upon reaching the interface with Coating A, the crack advanced along the A/B interface for up to several millimeters before kinking into the Coating A layer and completing its trajectory through the coating.

As noted in Section 2.1, Coating B is treated as a single layer analytically because its two constituent layers were composed of the same polymer and had nearly identical properties. This assumption is supported by observations that the crack path traveled smoothly across the interface between the two similar layers without disruption or a change in path (Fig. 10(b)). In contrast, for the two-layer Coating AB, the crack exhibited a pronounced change in path when it reached the interface between B and A layers (Fig. 10(c)).

Analytical predictions of θ_p are compared to experimental measurements of crack kink angle in Table 4 and Fig. 11. The error bars (sensitivity bands) for the analytical predictions show the effects of varying the Poisson's ratio ν of the coating material in which the crack is advancing by $\pm 10\%$. This is based on results of the sensitivity analysis described in Section 3.2, which showed that the analytically predicted crack path is most sensitive to Poisson's ratio and only weakly sensitive to elastic modulus. A $\pm 10\%$ variation in ν was selected based on a conservative estimate of experimental error in free-film measurements of Poisson's ratio, where actual experimental error is estimated at 7–10 %. For the experimental values, given that multiple measurements of crack kink angle were made on each pull stub, the average experimental measurement for each system/interface combination represents a pooled mean (i.e., the average for all pull stubs, where each pull stub value is itself an average of the measurements made on that individual pull stub). A few stubs and images were non-measurable due to poor visibility of the crack kink angles (examples: jagged cracking or coating peeling/liftoff). In all, a total of 1,305 valid crack kink angle measurements were made across 111 pull stubs in the sample set. Mean experimental crack kink angles were close to the analytical predictions for all four interfaces examined, and in all cases the experimental error bands included the analytical prediction value. This agreement is promising and supports the validity of the method.

4.2. Fracture pattern analysis via image segmentation

Fig. 12 shows a representative sample of stub micrographs for each coating system, illustrating the range of fracture patterns that were observed. Each stub image is a composite of four individual micrographs, each showing one quadrant of the stub. Fig. 13 shows the results of image segmentation for this representative micrograph set, using classifiers trained for each coating system in Trainable WEKA.

Fracture patterns that include high area fractions for *adhesive* and *exposed aluminum stub* are considered the best outcomes, since in those regions, the coating remained intact and adhered to the substrate panel. Fracture patterns that include high area fractions for the coating materials indicate inferior performance, since at least some of the coating was lifted from the panel with the stub. The segmented images facilitate both visual and quantitative assessments of how the coatings behaved in adhesion testing, including identification of materials and interfaces most vulnerable to decohesion. We assessed fractional area coverage of each material on the pull stubs by using a simple script in ImageJ to count the number of pixels in each color in the segmented images.

Quantitative image segmentation results are summarized in Fig. 14. Coating removal represented an average of 45 %, 32 %, and 91 % of stub area for Coatings A, B, and AB respectively, whereas the remaining stub area was coded as visible adhesive or exposed aluminum (i.e., without coating removal). These data suggest that Coating B offered the most desirable fracture pattern (least coating removed) while Coating AB offering the least desirable pattern (most coating removed). This visually driven assessment provides a useful accompaniment to other adhesion test data, particularly for coatings that yield similar adhesion strengths such as those in this study. All three coatings considered here performed nearly identically in adhesion strength testing, but nonetheless could be clearly ranked by desirability of the typical failure pattern.

5. Discussion and conclusions

Pull-off coating adhesion tests such as ASTM D4541 are popular field tests because they provide a rapid and portable assessment of a coating's adhesion strength; however, these tests have generally been assumed to be of limited value for fracture mechanics and mechanistic analysis. In this article, we offer a suggestion that the value of the pull-off adhesion test can be enhanced through simple yet rigorous post-test characterization of test stubs. We demonstrated two new methods for extracting analytically useful fracture data from pull-off adhesion test stubs:

- Crack path measurements can be used to estimate mode mixity, enabling disambiguation of mode-I and mode-II fracture.

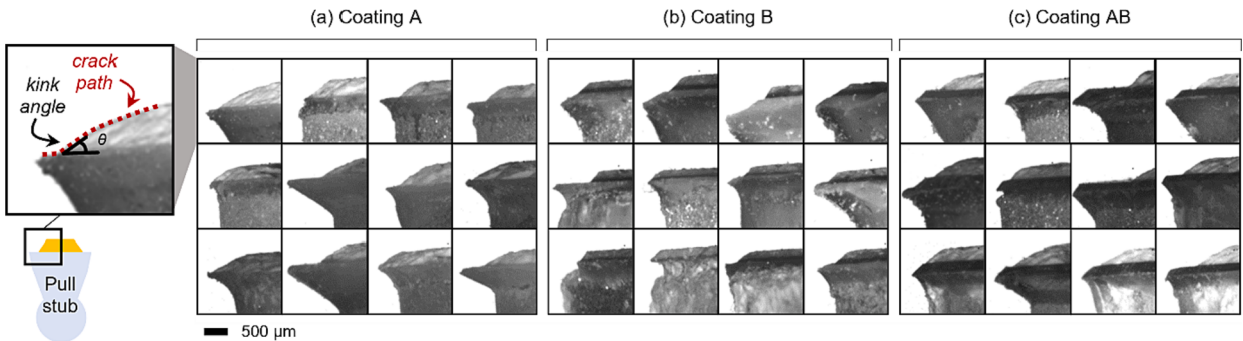


Fig. 10. Representative sample of side-view micrographs, revealing the angles at which the crack kinked into and through the coating in the fracture process, for (a) Coating A, (b) Coating B, and (c) Coating AB. In all, 1,305 valid crack kink angle measurements were made across 111 pull stubs (after excluding non-measurable specimens).

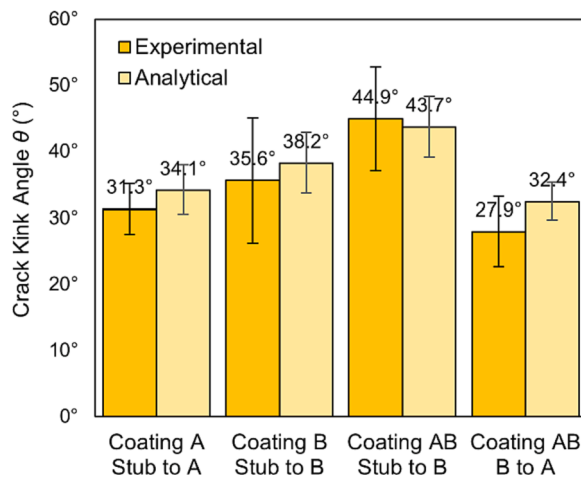


Fig. 11. Comparison of experimental measurements of crack kink angles to analytical predictions. For experimental measurements, error bars represent the standard deviation. For analytical predictions, error bars are based on sensitivity analysis and show the effects of varying Poisson's ratio (for the layer in which the crack is advancing) by $\pm 10\%$.

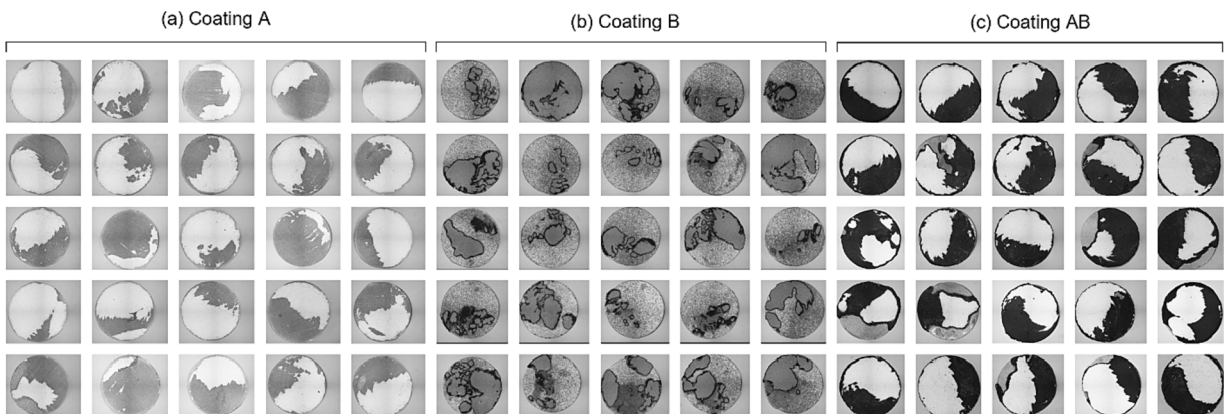


Fig. 12. Representative sample of top-view stub micrographs for (a) Coating A, (b) Coating B, and (c) Coating AB. Each micrograph shown is the composite of four individual images, each comprising one quadrant of the 20-mm-diam pull stub.

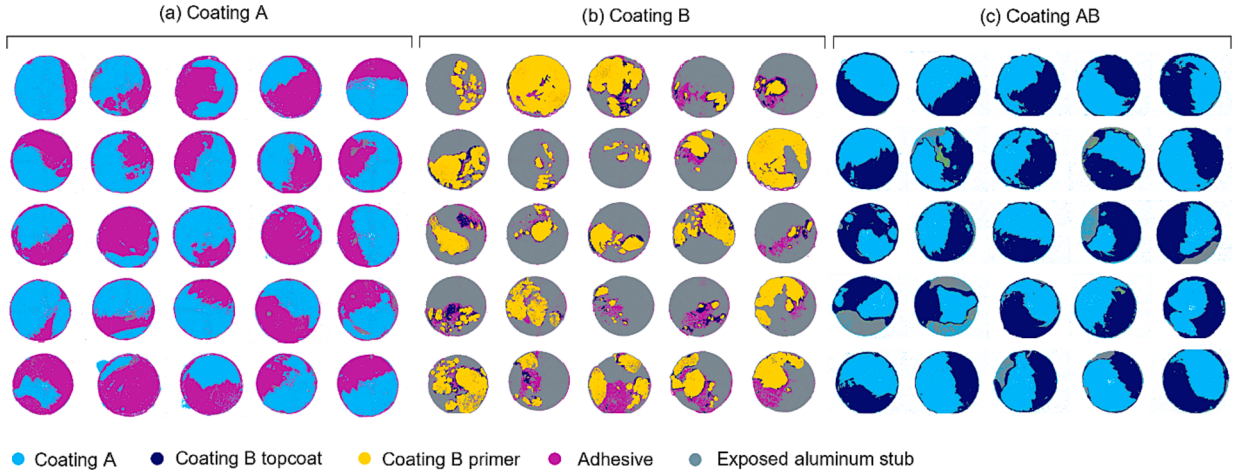


Fig. 13. Segmented images after classification in Trainable WEKA for (a) Coating A, (b) Coating B, and (c) Coating AB. Pull stubs correspond to those shown in Fig. 12.

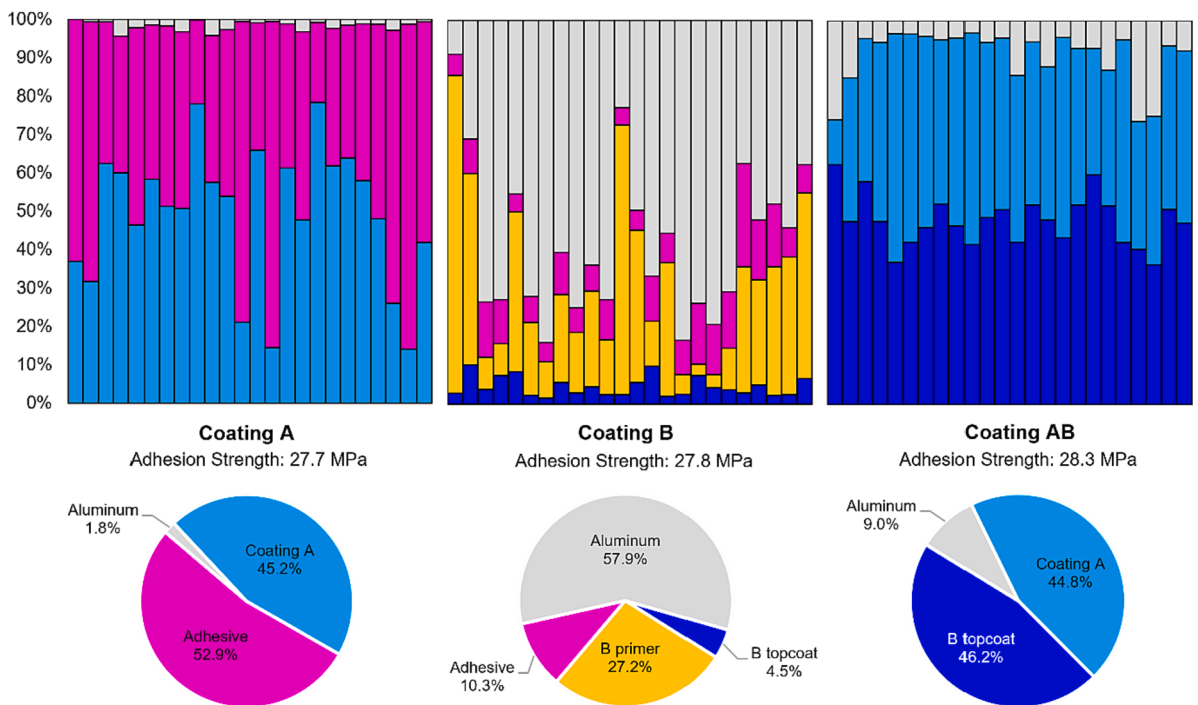


Fig. 14. Fractional area coverage of coating materials, adhesive, and exposed aluminum on post-test adhesion test stubs, as measured with machine-learning-based image segmentation. The bar charts show individual results for a representative set of pull stubs for each coating system. The pie charts below show the overall average area coverage result for all pull stubs from each coating system. All three coating systems exhibited nearly identical pull-off adhesion strengths.

- Image segmentation and analysis can enable identification of the most likely failure interfaces for a given coating and quantify the prevalence of different fracture behaviors. This can complement adhesion strength data for objective comparisons across coating systems—including amongst coating systems that exhibit similar adhesion strengths.

Techniques are demonstrated here for a standard pull-off adhesion test for which loading conditions are generally known; however they also have potential for extension to other situations where the loading conditions (or material properties) are unknown or uncertain. For example, plans for future work include leveraging the crack path measurement technique for the development and validation of new adhesion tests that incorporate twisting and different levels of mixed-mode loading. Crack kink angle measurement

techniques may also have potential for use in forensic failure analysis of delamination defects (i.e., to learn about the root cause of an observed coating decohesion). We also plan to broaden this work to consider additional coating types, including coatings exhibiting a broader range of tensile behavior. Further work is needed to understand the range of coating and system attributes for which this technique could be valid (beyond the brittle epoxies considered here). This will include an exploration of plasticity and non-linearity. We would expect plasticity effects to have increasing importance as the mode II loading component increases [18] compared to the predominantly mode-I loadings considered in this work.

We also plan to further explore the relationships between fracture toughness and mode mixity in different systems, and the impact of toughness on crack path, to understand the generality of this technique with respect to mode-mixity phase angle. Fracture toughness is known to be a function of the relative contributions of mode I to mode II fracture acting on the interface (see e.g. Refs. [17,19,20]) with increasing levels of mode II tending to toughen the interface (with some exceptions [21]). However, in a limited range of mode mixity, the toughness may be nearly constant. For example, Liechti and Chai [19] showed experimentally that fracture toughness was relatively independent of mode mixity for $0^\circ < \psi < 45^\circ$ in an epoxy/glass system, though toughness was sensitive to mode mixity beyond this range. The experiments reported here reflect a narrow subset of the constant-toughness range from Liechti and Chai's paper (i.e., $14^\circ < \psi < 23^\circ$ after correcting for length scale, as shown in Table 2). These are mode-I dominant loadings. Generality beyond this limited range of mode mixity (and fracture toughness) will be an important subject for future study.

This work suggests that the pull-off adhesion test, already popular for field testing, may be undervalued as a rigorous tool for fracture analysis. Further, the technique described here for estimating mode mixity from the crack path offers significant future potential as a useful tool for failure analysis in delaminated coating systems. Microscopy of used test stubs (in two dimensions) reveals a rich dataset from which we can draw mechanistic insights about fracture processes. The techniques presented in this paper offer examples of how microscopic images can be collected, measured, and interpreted to deepen understanding of coating adhesion and failure.

CRediT authorship contribution statement

Heather P.H. Liddell: Writing – review & editing, Writing – original draft, Visualization, Methodology, Investigation, Formal analysis, Conceptualization. **Laura M. Erickson:** Writing – review & editing, Resources, Methodology, Investigation. **James P. Tagert:** Investigation, Methodology, Writing – review & editing. **Attilio Arcari:** Writing – review & editing, Methodology, Investigation. **Gregory M. Smith:** Writing – review & editing, Investigation. **James Martin:** Supervision, Funding acquisition.

Declaration of Competing Interest

The authors declare that they have no known competing financial interests or personal relationships that could have appeared to influence the work reported in this paper.

Data availability

The authors do not have permission to share data.

Acknowledgments

Funding of this work by the Office of Naval Research through the U.S. Naval Research Laboratory (NRL) Basic Research Program (through the NRL Karles Fellowship and NRL American Society for Engineering Education (ASEE) Postdoctoral Fellowship) is gratefully acknowledged. We appreciate Dr. Chris Rudolf (of NRL) for assistance with measurement of Poisson's ratio for the free-film coatings using digital image correlation. Robert Kogler (of Rampart, LLC) and Dr. Edward Lemieux (of NRL) are thanked for their review and comments on this manuscript. We are grateful to Dr. Marriner Merrill (of NRL) for his support of this project including sharing of laboratory resources and equipment. Finally, H.L. wishes to express her appreciation to Prof. John C. Lambropoulos at the University of Rochester for correspondence and discussion that helped to shape the analytical portion of the work.

References

- [1] ASTM D4541-17: Standard Test Method for Pull-Off Strength of Coatings Using Portable Adhesion Testers. <http://doi.org/10.1520/D7234-21>.
- [2] Arganda-Carreras I, Kaynig V, Ruedon C, Eliceiri KW, Schindelin J, Cardona A, et al. Trainable Weka Segmentation: a machine learning tool for microscopy pixel classification. *Bioinformatics* 2017;33:2424–6. <https://doi.org/10.1093/bioinformatics/btx180>.
- [3] ASTM D882-00: Standard Test Method for Tensile Properties of Thin Plastic Sheetings. <http://doi.org/10.1520/D0882-00>.
- [4] Bauer CL, Farris RJ. Determination of Poisson's ratio for polyimide films. *Polym Engng Sci* 1989;29:1107–10. <https://doi.org/10.1002/pen.760291606>.
- [5] Shen S, Li H, Yang L, Li N, Wu J, Zao T. High throughput screening the micro-mechanical properties of polyimide matrix composites at elevated temperatures. *Polym Test* 2022;107:107583. <https://doi.org/10.1016/j.polymertesting.2022.107483>.
- [6] Qi D, Hinkley J, He G. Molecular dynamics simulation of thermal and mechanical properties of polyimide-carbon-nanotube composites. *Modell Simul Mater Sci Eng* 2005;13:493–507. <https://doi.org/10.1088/0965-0393/13/4/002>.
- [7] Tagert J, Martin J. Alternative Adhesion Test – Creep Test, presented at the Society for Protective Coatings Exhibition (SSPC) 2018, New Orleans, LA, January 15–18, 2018.
- [8] Budynas RG, Nisbett JK. Shigley's Mechanical Engineering Design. 8th edition (McGraw-Hill, 2006) Chapter 8.
- [9] Merrill MH, Reid RC, Gogotsi N, Thomas JP. Electrowetting on polyimide and silicon substrates with high hysteresis. *Microsyst Technol* 2018;24:4847–54. <https://doi.org/10.1007/s00542-018-3896-0>.

- [10] Liddell HPH, Merrill MH. In situ visualization of particle motions during wipe sampling of explosives and other trace particulate materials. *ACS Appl Mater Interfaces* 2019;11:23780–8. <https://doi.org/10.1021/acsami.9b06761>.
- [11] DeGreeff LE, Liddell HPH, Pogue II WR, Merrill MH, Johnson KJ. Effect of re-use of surface sampling traps on surface structure and collection efficiency for trace explosive residues. *Forensic Sci Int* 2019;297:254–64. <https://doi.org/10.1016/j.forsciint.2019.02.002>.
- [12] He M-Y, Hutchinson JW. Kinking of a crack out of an interface. *J Appl Mech* 1989;56:270–8. <https://doi.org/10.1115/1.3176078>.
- [13] Masabe R, Ustinov K, Barbieri L, Berggreen C. Fracture mechanics solutions for interfacial cracks between compressible thin layers and substrates. *Coatings* 2019;9:152. <https://doi.org/10.3390/coatings9030152>.
- [14] He M-Y, Hutchinson JW. Kinking of a crack out of an interface: tabulated solution coefficients. (Harvard University; 1989. Technical Report MECH-113A.
- [15] Thouless MD. Cracking and delamination of coatings. *J Vac Sci Technol A* 1991;9:2510. <https://doi.org/10.1116/1.577265>.
- [16] Liddell HPH, Mehrotra K, Lambropoulos JC, Jacobs SD. Fracture mechanics of delamination defects in multilayer dielectric coatings. *Appl Opt* 2013;52:7689–98. <https://doi.org/10.1364/AO.52.007689>.
- [17] Hutchinson JW, Su Z. Mixed mode cracking in layered materials. *Adv Appl Mech* 1992;29:63–191. [https://doi.org/10.1016/S0065-2156\(08\)70164-9](https://doi.org/10.1016/S0065-2156(08)70164-9).
- [18] Tvergaard V, Hutchinson JW. The influence of plasticity on mixed mode interface toughness. *J Mech Phys Solids* 1993;41:1119. [https://doi.org/10.1016/0022-5096\(93\)90057-M](https://doi.org/10.1016/0022-5096(93)90057-M).
- [19] Liechti KM, Chai YS. Asymmetric shielding in interfacial fracture under in-plane shear. *J Appl Mech* 1992;59:295. <https://doi.org/10.1115/1.2899520>.
- [20] Volinsky AA, Moody NR, Gerberich WW. Interfacial toughness measurements for thin films on substrates. *Acta Mater* 2002;50:441. [https://doi.org/10.1016/S1359-6454\(01\)00354-8](https://doi.org/10.1016/S1359-6454(01)00354-8).
- [21] Dillard DA, Singh HK, Pohlit DJ, Starbuck JM. Observations of decreased fracture toughness for mixed mode fracture testing of adhesively bonded joints. *J Adhes Sci Technol* 2009;23:1515–30. <https://doi.org/10.1163/156856109X452701>.